Journal Pre-proof

Adaptive spectral band integration in flash thermography: Enhanced defect detectability and quantification in composites

Gaétan Poelman, Saeid Hedayatrasa, Joost Segers, Wim Van Paepegem, Mathias Kersemans

PII: S1359-8368(20)33355-2

DOI: https://doi.org/10.1016/j.compositesb.2020.108305

Reference: JCOMB 108305

To appear in: *Composites Part B*

Received Date: 28 April 2020

Revised Date: 7 July 2020

Accepted Date: 13 July 2020

Please cite this article as: Poelman Gaé, Hedayatrasa S, Segers J, Van Paepegem W, Kersemans M, Adaptive spectral band integration in flash thermography: Enhanced defect detectability and quantification in composites, *Composites Part B* (2020), doi: https://doi.org/10.1016/j.compositesb.2020.108305.

This is a PDF file of an article that has undergone enhancements after acceptance, such as the addition of a cover page and metadata, and formatting for readability, but it is not yet the definitive version of record. This version will undergo additional copyediting, typesetting and review before it is published in its final form, but we are providing this version to give early visibility of the article. Please note that, during the production process, errors may be discovered which could affect the content, and all legal disclaimers that apply to the journal pertain.

© 2020 Published by Elsevier Ltd.

7 July 2020

Dear Editors-in-Chief of Composites Part B: Engineering,

This is to certify that all authors of the manuscript "*Adaptive spectral band integration in flash thermography: Enhanced defect detectability and quantification in composites*", by Gaétan Poelman, Saeid Hedayatrasa, Joost Segers, Wim Van Paepegem and Mathias Kersemans, have agreed with its publication by Composites Part B: Engineering and have no conflict of interest in the subject matter or materials discussed in this manuscript.

With best regards,

Gaétan POELMAN

GHENT UNIVERSITY
FACULTY OF ENGINEERING AND ARCHITECTURE

ir. Gaétan Poelman
Doctoral student – NDT of composites by thermography
FWO Aspirant Strategic Basic Research
T +32 (0)9 331 04 34

Mechanics of Materials and Structures
Department of Materials, Textiles and Chemical Engineering
Technologiepark 46, B-9052 Zwijnaarde (Gent), Belgium

Journal Pre-proof

Adaptive spectral band integration in flash thermography: Enhanced defect detectability and quantification in composites

Gaétan Poelman [1,*], Saeid Hedayatrasa [1,2], Joost Segers [1], Wim Van Paepegem [1] and Mathias Kersemans [1]

[1] Mechanics of Materials and Structures (UGent-MMS), Department of Materials, Textiles and Chemical Engineering, Ghent University, Technologiepark-Zwijnaarde 46, 9052 Zwijnaarde, Belgium

[2] SIM Program M3 DETECT-IV, Technologiepark-Zwijnaarde 48, B-9052 Zwijnaarde, Belgium

[*] Corresponding author: Gaetan.Poelman@UGent.be

Abstract

In flash thermography, the maximum inspectable defect depth is limited when only the raw thermographic sequence is analyzed. The introduction of pulsed phase thermography (PPT), in which phase (contrast) images at different thermal wave frequencies are obtained, significantly improved the maximum inspectable depth while reducing the effects of non-uniform heating and non-uniform surface properties. However, in a practical environment, the evaluation of many phase images per inspection is a cumbersome procedure.

In this paper, a novel Adaptive Spectral Band Integration (ASBI) procedure is introduced for the post-processing of flash thermographic datasets, which yields a unique damage index map. ASBI integrates the most useful spectral information for each pixel individually, obtaining a maximized defect detectability and an almost zero-reference level. The performance of ASBI with respect to defect detectability as well as defect sizing and depth inversion is evaluated thoroughly with both experimentally and numerically generated datasets. The ASBI procedure is successfully applied on various composite coupons with flat bottom holes and barely visible impact damage, as well as on a stiffened aircraft composite panel with a complex cluster of production defects. The ASBI procedure is compared with existing data-processing techniques in literature, illustrating an enhanced performance.

Keywords: Non-destructive testing (NDT), Flash thermography, Data processing, Fourier analysis, Composites, GFRP, CFRP, Barely visible impact damage (BVID)

1. Introduction

In recent years, composites have gained a lot of attention from industry due to their advantageous properties, such as a high stiffness-to-weight ratio and good corrosion resistance in comparison to traditional metals. However, these composite materials are susceptible to the formation of internal damage features due to their layered structure. These internal defects tend to grow over time and may jeopardize the structure's mechanical integrity. Since composites are widely implemented in high-end applications (e.g. up to 50% of modern aircrafts consists of composites), advanced non-destructive testing (NDT) is required to provide early defect detection to guarantee their structural integrity.

Flash thermography (FT) is a popular NDT technique in which defective regions are visualized by exploiting the local difference in the thermal properties between a defect and its surrounding sound material [1-5]. In FT, a short but intense flash excitation is used to induce a thermal imbalance throughout the sample's thickness, causing thermal waves to diffuse into the material's thickness. Meanwhile, the temporal evolution of the excited surface's temperature is

Journal Pre-proof

recorded using an infrared (IR) camera. At internal defect boundaries, the heat diffusion is impeded, leading to a locally increased temperature in the recorded thermal sequence. However, flash thermography is inherently limited by the highly diffusive and strongly damped nature of the induced thermal waves, making the accurate detection of small and deep defects very challenging. Several image processing techniques, which only use the input of one single thermogram, have been developed to enhance the defect detectability by reducing noise and background non-uniformities [6-8]. Also many data post-processing techniques, which use the complete recorded thermographic sequence, have been implemented to further enhance the defect detectability [1, 9-12].

Pulsed phase thermography (PPT) was introduced as one of the first advanced data processing techniques, in which each pixel's thermal sequence is decomposed into its harmonic components by applying the fast Fourier transform (FFT) [13]. The output of the FFT procedure yields amplitude and phase images that govern a wide frequency range, which is dependent on the recording settings, i.e. total recording duration and sampling frequency [13, 14]. Typically, only the phase images are evaluated for NDT since they are emissivity-normalized, meaning that the adverse effects of background non-uniformity and non-uniform surface properties are reduced [14]. Thus, phase images have a more uniform background than the corresponding amplitude images. Additionally, the evaluation frequency is inversely proportional to the inspection depth, i.e. a thermal wave with a lower evaluation frequency has a higher diffusion length and provides a deeper probing into the material. Hence, a unique evaluation frequency that provides optimal detection for defects at different depths does not exist. As such, the required full-thickness inspection of a component calls for the assessment of multiple frequencies, which is a cumbersome evaluation procedure.

Besides the well-known PPT technique, there exist several other well-known data processing techniques for FT in both time and frequency domain, such as Differential Absolute Contrast (DAC) [15, 16], Principal Component Thermography (PCT) [17], Thermographic Signal Reconstruction (TSR) [18-20] and Dynamic Thermal Tomography (DTT) [21]. In DAC, the behavior of each pixel in its sound state is estimated by applying an idealized 1D solution for the heat diffusion equation. By calculating the thermal contrast between the measured signal and the estimated sound behavior, a reference-free thermal contrast technique is thus obtained. In PCT, the recorded dataset size is significantly reduced by projecting it onto a statistical orthogonal base which provides the strongest projection. This leads to a set of principal components, which captures most of the observed variability (e.g. due to the presence of defects) in the recorded thermographic sequence. TSR fits a low-order polynomial function to each pixel's cooling regime in loglog-space, for which then only the polynomial coefficients need to be stored. This technique therefore strongly reduces the data size and measurement noise. Alternatively, the first and second order derivatives of the polynomial fit may be used for improved defect detectability and for defect depth estimation. In DTT, each pixel is represented by the value and the time instance of its maximum thermal contrast, generating a 'maxigram' and 'timegram', respectively. Next, a correlation function can be constructed to convert the timegram values into quantitative depth information. More recently, Thermal Signal Area (TSA) [22] has been introduced which performs an integration of the raw surface temperature over a user-defined temporal range in order to obtain an improved defect detectability.

Besides enhancing a defect's detectability, it is also desired to obtain quantitative information on its size and depth location. Accurate defect sizing is significantly complicated in infrared thermography due to the lateral heat diffusion. Several approaches have been introduced for optical infrared thermography, such as full-width at half-height [23] and shearing-phase profiles

Journal Pre-proof

[24]. However, a consensus on the optimal approach has not yet been reached. On the other hand, in the field of ultrasonic NDT, the drop technique is a standard technique for defect size estimation, in which a defect is sized by applying a cut-off at a specific percentage of the defect's maximum amplitude [25-27]. For FT, several procedures for defect depth estimation have been introduced [21, 28-34], most of which rely on the idealized 1D solution for the heat diffusion equation or on artificial neural networks. With respect to PPT, it is known that there does not exist an unambiguous relationship between the phase angle and the defect depth [30], which means that individual phase (contrast) images cannot be used for proper depth inversion. However, there does exist a well-known inverse relationship between the defect depth and the second blind frequency [9, 14, 35]. At this second blind frequency, a defect can typically no longer be distinguished from its surroundings based on the phase contrast because the signal has reached the noise level; the defect thus becomes 'blind' at this frequency [14, 36]. However, for glass fiber reinforced polymers, there is often a positive phase contrast after the second blind frequency, and there thus even exists a third blind frequency.

In this paper, we propose a novel data processing technique called Adaptive Spectral Band Integration (ASBI), in which relevant phase images are integrated in a pixel-wise manner in frequency domain, leading to a unique damage index map. This has particular advantages in terms of (i) emissivity normalization (reducing the effect of non-uniform heating and background reflections), (ii) signal-to-noise ratio (SNR) and (iii) probing depth. This damage index map can then further also be used for quantitative depth inversion by the use of a suitable correlation function. The structure of the remainder of this paper is as follows: section 2 describes the samples that were tested and the experimental procedure for this research paper. Section 3 provides a background on PPT and elaborates on its advantages, limitations and challenges. Next, the ASBI algorithm is introduced in section 4, and its performance is compared with both PPT and TSA. In section 5, the performance of ASBI towards quantitative defect depth inversion is evaluated, and compared with the approach based on PPT's second blind frequency (based on FE results). In section 6, ASBI is applied and demonstrated on two challenging inspection cases: (i) a composite coupon with barely visible impact damage, and (ii) a stiffened aerospace component with a complex cluster of production defects. Finally, section 7 gathers the concluding remarks.

2. Materials and methods

A glass fiber reinforced polymer (GFRP; an often-used material in the wind industry) coupon with FBHs, a carbon fiber reinforced polymer (CFRP) coupon with barely visible impact damage (BVID), and a stiffened CFRP aircraft panel with production defects are investigated.

The GFRP sample is a square 200x200 mm^2 plate with a total thickness of 5 mm and a cross-ply $[(0/90)_5]_s$ layup, and is used to introduce the different steps involved in the ASBI procedure. Circular flat bottom holes (FBHs) with a diameter of 15 mm were milled from the back side of the sample, with a spacing in between the FBHs of 20 mm. The remaining material thicknesses at the defect locations range from 0.25 to 4 mm. A picture of the sample is provided in Figure 1(a). Additionally, two similar square GFRP samples (same size, thickness, stacking sequence and FBH depths) but with FBHs of diameter 10 mm (FBH spacing of 15 mm) and 5 mm (FBH spacing of 10 mm) are inspected.

The CFRP sample with BVID has a quasi-isotropic layup of $[(+45/0/-45/90)_3]_s$, and measures 140x90x5.5 mm^3. The sample was impacted by dropping a 7.72 kg impactor from a height of 0.3 m (measured impact energy of 18.5 J) using a calibrated drop tower, introducing barely visible

impact damage (BVID) [37]. A photograph of the impacted CFRP sample is provided in Figure 1(b).

The last sample is a CFRP panel with backside stiffeners that was manufactured for an Airbus A400M lower flap (see Figure 1(c)). It was scrapped based on the ultrasonic inspection performed by the manufacturer (inspection data is not available). The zone that contains production defects is hatched in the figure while the region indicated as 'inspected area' is investigated for the presence of defects. The panel consists of a skin plate of 500x1000x2.55 mm^3 with several backside stiffeners along the horizontal direction.

The samples are excited by a Hensel linear flash lamp which generated a 5 ms optical excitation with an energy of 6 kJ. For the GFRP sample, the cooling down regime was recorded for 180 s at a sampling frequency of 10 Hz with a FLIR A6750sc infrared (IR) camera in reflection mode. For the CFRP sample with BVID, the recording duration and sampling frequency were 45 s and 50 Hz, respectively. The aircraft panel was recorded for 40 s at 25 Hz. For the GFRP sample, a long recording time was adopted since this sample is used to introduce the ASBI algorithm and to compare it with PPT (where the frequency resolution is critical [14]). The CFRP samples were recorded with higher sampling frequencies, and for a shorter duration (i.e. until reaching the noise level) to limit the data size. The IR camera has a focal plane array of 640x512 cryo-cooled InSb detectors, which have a noise-equivalent differential temperature (NEDT) of ≤ 20 mK, and is sensitive within the 3-5 μm range. The distance between the flash lamp and each inspected sample was ~300 mm, while the IR camera was placed ~900 mm away for the GFRP sample, ~500 mm for the CFRP sample with BVID and ~1000 mm for the aircraft panel. The synchronization between the excitation and data acquisition was guaranteed through hard- and software from Edevis GmbH. The recorded thermographic sequences were imported into an in-house developed MATLAB toolbox for the post-processing.

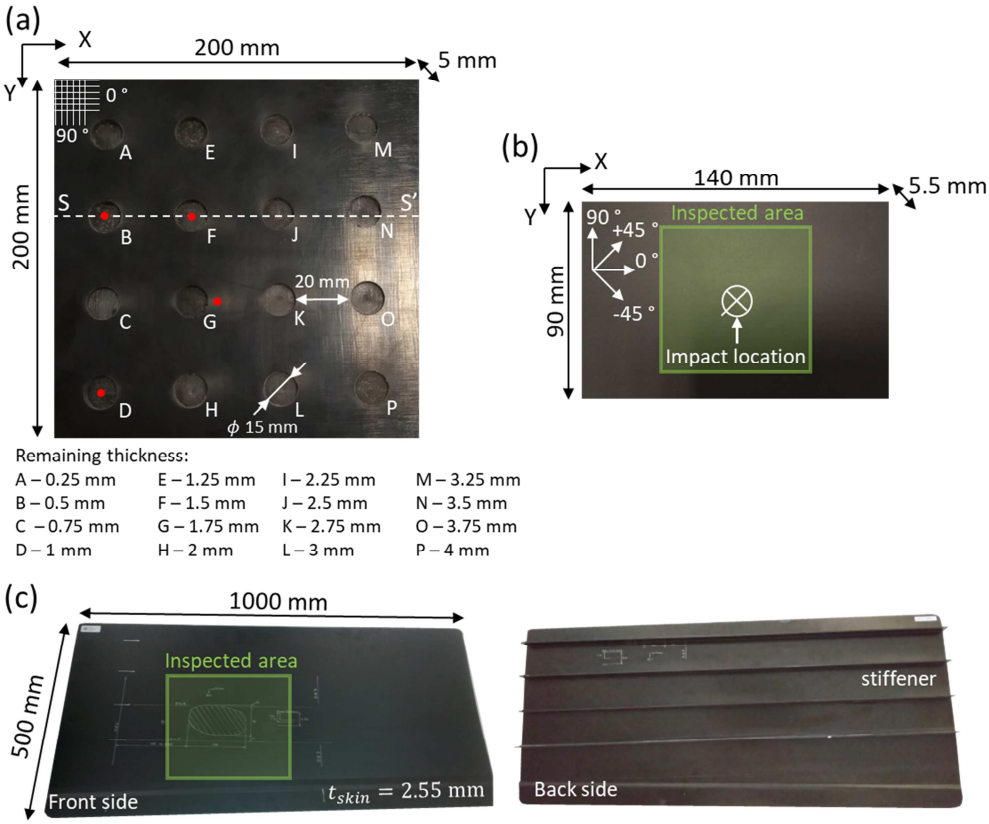

Journal Pre-proof

Figure 1: Schematic drawing of the (a) GFRP coupon with FBHs; (b) CFRP coupon with BVID; and (c) CFRP aircraft panel with backside stiffeners and production defects.

3. Background of pulsed phase thermography (PPT)

In pulsed phase thermography (PPT), first, amplitude and phase images are calculated for a wide range of frequencies through the application of the Fourier transform [9, 13, 14]. Next, the phase contrast $\Delta\varphi(f)$ is calculated for each frequency by subtracting the phase of a sound reference pixel. However, the selection of such a reference pixel is often non-trivial since it requires a priori information about the sample and its defects. As a practical alternative, the average phase value of the entire sample can also be used as reference value [28]. In this paper, the phase contrast is calculated according to the latter manner. This means that, if defects are present in the sample, the average phase angle of the entire sample will be more negative than the sound pixels' phase angle itself (since defects have a more negative phase angle than sound pixels). This then results in an initially positive phase contrast for sound pixels and a negative phase contrast for defected pixels.

Figure 2 presents the phase contrast curves for three FBHs at different defect depths and for a sound pixel. The four pixels are indicated with red dots in Figure 1(a). The sound pixel's behavior is governed by an initially positive phase contrast (since the entire sample was used for the reference phase angle) and by noisy fluctuations around the zero phase contrast. For the defects, the range of frequencies that exhibit a negative phase contrast is wider for shallower defects than for deeper defects. Additionally, the most shallow defect (FBH_B) exhibits the most negative phase contrast. This value gradually decreases with increasing defect depth. This is in accordance with the results in [4, 14, 20, 28]. For each defect, there exists a frequency of maximum negative phase contrast $f_{\Delta\varphi,max}$, which is dependent on the defect's depth and size (also observed in [4, 14, 20]). This entails that there does not exist one unique frequency that provides the optimal detection for all defects. Also, assessing only one frequency should be avoided since this evaluation frequency – while optimal for one defect – might correspond to a blind frequency of another defect, which would make that this particular defect remains undetected. As such, phase contrast images at multiple frequencies must be evaluated to obtain a through-depth inspection of the entire sample, which is often a cumbersome task. In the figure, the indicative phase contrast area of FBH_B is highlighted in green, which is defined by the frequency range where the defect's phase contrast is negative and by the maximum phase contrast $\Delta\varphi_{max}$.

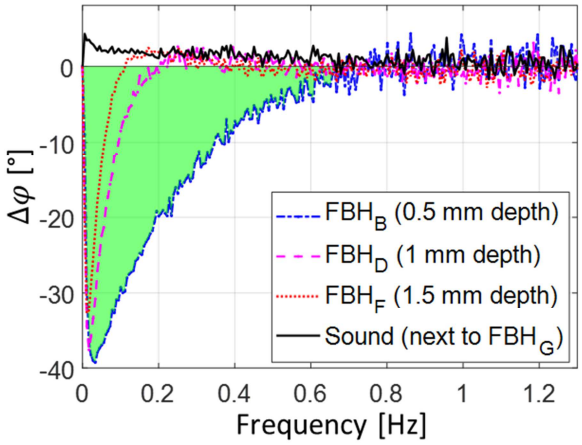

Figure 2: Phase contrast in function of frequency (the considered pixels are indicated by the red dots in Figure 1(a)).

Journal Pre-proof

4. Adaptive spectral band integration (ASBI)

The first part of this section is devoted to the introduction of the ASBI algorithm, after which ASBI is applied on the GFRP sample with FBHs (Figure 1(a)). Its performance is compared with the output of PPT and TSA.

4.1. Algorithm

Figure 3(a) provides a schematic overview of the phase contrast curve for a defected pixel, whereas Figure 3(b) plots the phase contrast curve for a sound pixel. Notice that for a shallow defected pixel, a positive phase contrast may arise at low evaluation frequencies due to 3D heat diffusion effects [36, 38]. In this case, the heat wave that is normally reflected from a (shallow) defect is predominantly dissipated through lateral heat diffusion at very low frequencies [38]. This thus introduces a first zero-crossing (ZC_1) before the maximum phase contrast is reached, as depicted in Figure 3(a). In order to avoid possible confusion, we call the (first) zero-crossing introduced by the defect's initial positive phase contrast '*first blind frequency*' $f_{blind,1}$, and the (second) zero-crossing that corresponds to the frequency at which the defect's phase contrast reaches the noise level (or crosses towards a positive phase contrast as in Figure 3(a)) '*second blind frequency*' $f_{blind,2}$ (see Figure 3(a)).

The first step of the ASBI algorithm is to define appropriate limits for the integration of the spectral information for each pixel, such that a unique damage index map is obtained. Considering the typical high-frequency noise due to the low involved energy [20] (see Figure 3(a,b)), integrating over the entire frequency range is not an effective option and would lead to erroneous results. As such, the proper range for the integration needs to be defined in a pixel-wise manner. In ASBI, the integration limits are defined by the range of the frequency domain where the pixel's phase contrast is negative (with the second blind frequency $f_{blind,2}$ as upper limit), hatched in green in Figure 2 and Figure 3(a,b). The definition of this integration domain can be simplified by setting all occurrences of a positive phase contrast ($\Delta\varphi(f) > 0$) equal to zero, as schematically indicated in Figure 3, which would then allow to integrate from 0 Hz up to the second blind frequency $f_{blind,2}$.

First, the second zero-crossing (ZC_2), which is the highest frequency that will be considered for the respective pixel (see Figure 3(a,b)), is located. This will either correspond to $f_{blind,2}$ or to a subsequent zero-crossing in the noisy regime. Following, the frequency bin at which the maximum negative phase contrast occurs, $f_{\Delta\varphi,max}$, is determined in the range from 0 Hz up to ZC_2. Sequentially, the second blind frequency $f_{blind,2}$ is found by searching for the first zero-crossing at a frequency higher than $f_{\Delta\varphi,max}$. With this procedure the second blind frequency $f_{blind,2}$ for ASBI is robustly extracted in an algorithmic manner. When there is no initial positive phase contrast, $f_{blind,2}$ corresponds to the first zero-crossing ZC_1. If there is an initial positive phase contrast, it will correspond to ZC_2. For shallow defects, this procedure might slightly underestimate $f_{blind,2}$ due to measurement noise since the slope of the phase contrast is very low in that region. Performing a polynomial fitting to reduce the measurement noise is, however, not recommended. The highly different phase contrast curves for different defect depths (see Figure 2) makes that performing an appropriate fitting for all pixel types at once is not feasible. Further, the added accuracy does not outweigh the added calculation costs. It is furthermore explicitly demonstrated in section 5.2 that this underestimation has no significant influence on the outcome of ASBI.

With the determined frequency range of interest for each pixel $p^{(i,j)}$, i.e. $\left[0\ \text{Hz} \dots f_{blind,2}^{(i,j)}\right]$, the following step is to integrate the useful phase spectral information inside this range. The damage index map DI at pixel $p^{(i,j)}$ is thus calculated as:

$$DI(i,j) = \sum_{f=0\ Hz}^{f_{blind,2}^{(i,j)}} \Delta\varphi(i,j,f)|_{\Delta\varphi(i,j,f)<0} \tag{1}$$

This corresponds to the integration of the green area in Figure 2 and Figure 3. Naturally, when inspecting a sound sample, ASBI provides a noisy image in which all pixels are governed by low phase angles, span a small integration range, and occur at random locations.

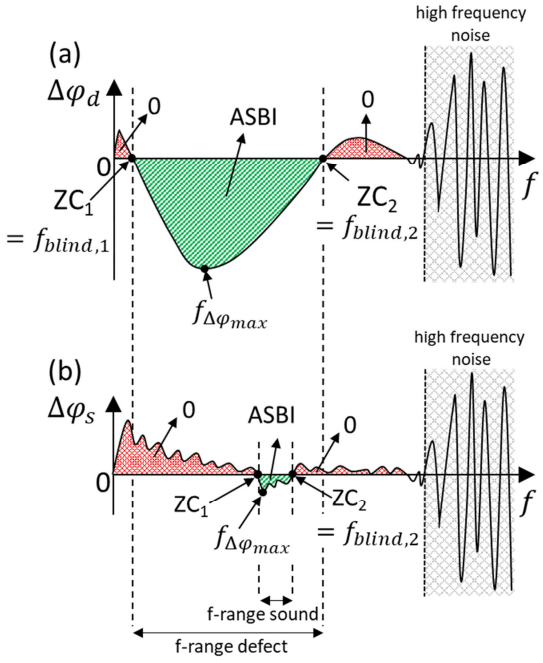

Figure 3: Schematic illustration of the ASBI algorithm: (a) phase contrast of a (shallow) defected pixel with initial positive phase contrast; (b) phase contrast of a sound pixel.

4.2. Comparison of PPT and ASBI

Figure 4 presents a comprehensive comparison for the GFRP coupon sample between individual phase contrast images obtained through the PPT algorithm and the damage index map calculated by ASBI. For better presentation of the results, a logarithmic scale has been employed.

In Figure 4(a), the phase contrast map is displayed for the frequency of maximum negative phase contrast for FBH_B ($f_{\Delta\varphi,max}^{B} = 0.03$ Hz). Notice that a logarithmic scale is used to represent the results. First, the sign of the phase contrast map is flipped, after which all phase contrast values are made positive by adding the minimal value of this resulting phase contrast map. Next, the decimal logarithm is taken. At this frequency, many of the deeper defects are not detected, and there is a significant amount of noise [20]. Additionally, a cross-section S-S' through the second row of FBHs (B, F, J and N in Figure 1(a)) is investigated, which is plotted in

Journal Pre-proof

Figure 4(b). The signal-to-noise ratio (SNR) of each of these FBHs is calculated based on the formula [39-41]:

$$SNR = 20\log_{10}\left(\frac{\left|\mu_{A_d} - \mu_{A_{ref}}\right|}{\sigma_{A_{ref}}}\right) \quad \text{(dB)} \tag{2}$$

where μ_{A_d} and $\mu_{A_{ref}}$ are the average values of the defected and reference sound areas (respectively A_d and A_{ref} in Figure 4(a)), and $\sigma_{A_{ref}}$ is the standard deviation of the reference sound area A_{ref}. The area for A_d measures 21x21 pixels and 25x364 pixels for A_{ref}. The obtained SNR values of the FBHs are indicated on the cross-sectional plot. The two shallowest defects of S-S' are clearly detected with high SNR levels, while the third defect shows a reduced contrast and the deepest defect exhibits a slightly positive phase contrast (i.e. the frequency is higher than the second blind frequency for this defect). Also, the background in between the defects is non-uniform and noisy.

Lowering the evaluation frequency to the frequency of maximum phase contrast for FBH_F ($f^F_{\Delta\varphi,max} = 0.01$ Hz) provides detection of deeper defects, but the signatures of the (shallower) defects are enlarged due to the increased effect of lateral heat diffusion at this lower frequency (see Figure 4(c)). The background of the phase contrast map is less uniform at this lower frequency, while the phase contrast of the shallow defects has decreased in comparison to $f^B_{\Delta\varphi,max}$ (see also Figure 2). The detectability of all FBHs is high, which is evidenced by the high corresponding SNR values in Figure 4(d).

Figure 4(e) displays the output from the proposed ASBI algorithm, which is also presented in a logarithmic scale (calculated in a similar manner as the phase contrast images). In this figure, all defects are consistently detected and an almost zero-reference background is obtained. The highest damage index is obtained for the most shallow defect FBH_A, which is logical since the frequency range of interest $\left[0\text{ Hz} \ldots f^A_{blind,2}\right]$ is wider and the phase contrast is higher (in absolute values) for shallower defects. Additionally, ASBI effectively enhances the defect contrast and reduces the background non-uniformity and noise level in comparison to the individual phase contrast images. Lastly, Figure 4(f) illustrates the cross-section S-S' for the output from ASBI, in which it is clear that the SNR of each defect is significantly higher than for any of the individual phase contrast maps at $f^B_{\Delta\varphi,max}$ and $f^F_{\Delta\varphi,max}$ (Figure 4(b,d)).

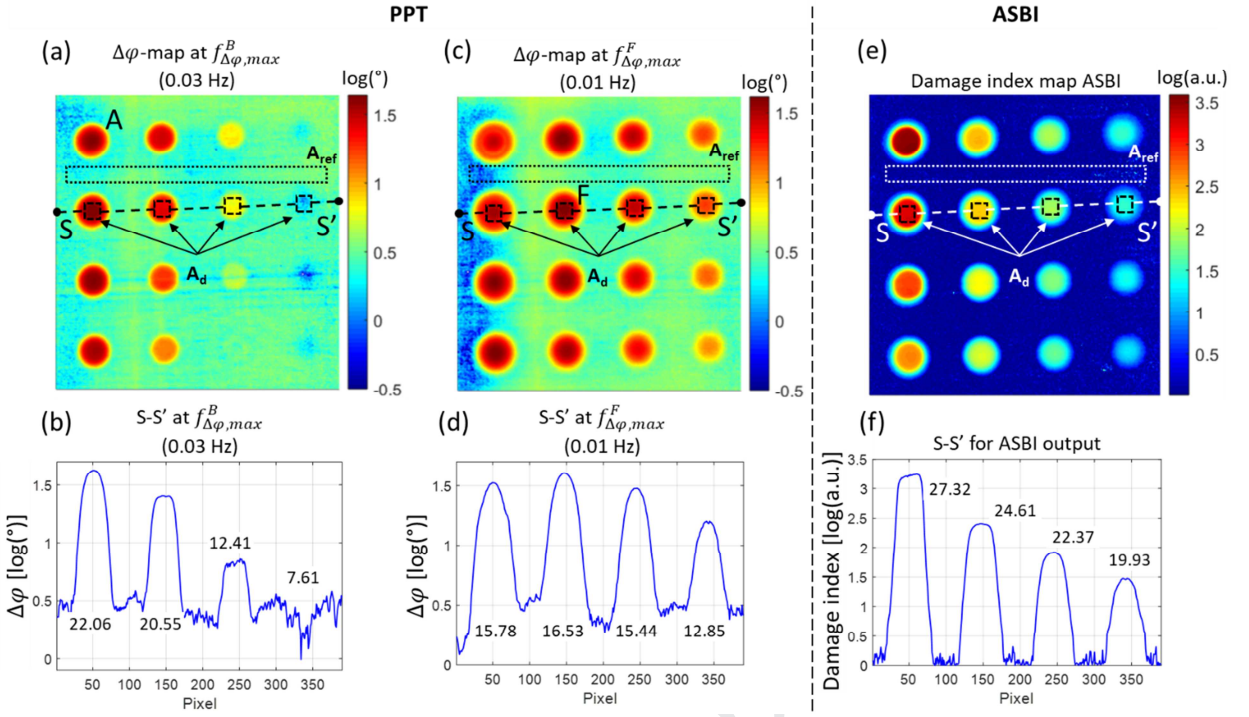

Figure 4: (a-d) phase contrast map and cross-section S-S' at the frequency of maximum phase contrast for FBH_B and FBH_F , $f^B_{\Delta\varphi,max}$ and $f^F_{\Delta\varphi,max}$, respectively; (e,f) damage index map of ASBI and cross-section S-S'. The plots of the cross-section S-S' (b,d,f) contain indications of the defects' SNR values (in dB).

An overview of the SNR values of all FBHs is presented in Table 1, in which the reference area A_{ref} (see Figure 4) was used for each FBH. The SNR for both PPT (at $f_{\Delta\varphi,max}$) and ASBI decreases steadily with increasing defect depth. The results also suggest that, independent of the defect depth, ASBI provides an enhanced defect detectability over PPT's maximum phase contrast $f_{\Delta\varphi,max}$.

Table 1: SNR values for all FBHs of the GFRP sample with diameter of 15 mm (see Figure 1(a)) for PPT (at $f_{\Delta\varphi,max}$), TSA and ASBI.

SNR of all FBHs [dB]
($\phi = 15$ mm)

	Depth [mm]	PPT (at $f_{\Delta\varphi,max}$)	TSA (0-50 s)	ASBI		Depth [mm]	PPT (at $f_{\Delta\varphi,max}$)	TSA (0-50 s)	ASBI
FBH_A	0.25	22.60	17.81	28.13	FBH_I	2.25	15.45	6.38	22.44
FBH_B	0.5	22.06	15.61	27.32	FBH_J	2.5	15.44	5.85	22.37
FBH_C	0.75	21.31	14.95	26.37	FBH_K	2.75	15.02	3.81	21.78
FBH_D	1	18.28	13.90	25.51	FBH_L	3	13.79	2.48	21.10
FBH_E	1.25	18.15	16.85	24.88	FBH_M	3.25	13.56	-13.43	20.00
FBH_F	1.5	16.53	16.15	24.61	FBH_N	3.5	13.49	-6.91	19.93
FBH_G	1.75	16.38	14.62	23.88	FBH_O	3.75	13.04	-1.00	19.12
FBH_H	2	16.06	12.95	23.25	FBH_P	4	12.29	1.05	18.08

An overview of the estimated lateral sizes of FBH_B and FBH_F (actual diameter of $\phi = 15$ mm) in function of the frequency is presented in Figure 5(a) for the -3 dB drop technique (i.e. cut-off at 50% of a defect's maximum amplitude). It was found earlier that the -3 dB drop technique often underestimates a defect's size in infrared thermography [24], which is also illustrated in the figure. The estimation for the shallow FBH_B is quite stable over the evaluated frequencies (except at the lowest frequency bin), having an error in defect sizing of about -11% at its optimal evaluation frequency $f^B_{\Delta\varphi,max}$. The deeper FBH_F has a defect sizing error of -8% at its

optimal evaluation frequency $f^F_{\Delta\varphi,max}$. The defect size estimation with ASBI is in the same range, having an error of about -6% for FBH_B and -8% for FBH_F.

Additionally, the estimated lateral sizes of FBH_B and FBH_F (actual diameter of $\phi = 15$ mm) through the -6 dB drop technique (i.e. cut-off at 25% of a defect's maximum amplitude) are presented in Figure 5(b). Notice that in this case, the defect sizes are generally overestimated. The estimation of the size of the shallow FBH_B from the phase contrast images is quite accurate at relatively high frequencies and becomes worse with decreasing evaluation frequency (+25% error in defect sizing at $f^F_{\Delta\varphi,max}$, and about +8% error at its optimal $f^B_{\Delta\varphi,max}$). The deeper FBH_F on the other hand is sized more accurately for all presented evaluation frequencies, but also significantly deviates from the real value ($\phi = 15$ mm) at its frequency of maximal phase contrast $f^F_{\Delta\varphi,max}$ (+17% error at its optimal $f^F_{\Delta\varphi,max}$ and +3% error at $f^B_{\Delta\varphi,max}$). Hence, the optimal frequency for defect detectability does not necessarily correspond to the frequency that provides the most accurate size estimation (for both the -3 dB and -6 dB drop technique). This further complicates the evaluation procedure through different phase contrast images in PPT. In contrast, estimating the defect size based on ASBI's damage index with the -6 dB drop technique provides improved results, with only a minimal overestimation for the deepest FBH_F (0% error for FBH_B and about +8% error for FBH_F). For ASBI, the frequency range of [$f_{\Delta\varphi,max}$, $f_{blind,2}$] provides the main contribution to the damage index since it covers considerably more frequency bins than the frequency range [0 Hz, $f_{\Delta\varphi,max}$] (see Figure 2). Since the main contributors are those frequencies that are less affected by lateral heat diffusion (i.e. the higher frequencies, see Figure 5), the defect sizing by ASBI is therefore more accurate than by $f_{\Delta\varphi,max}$.

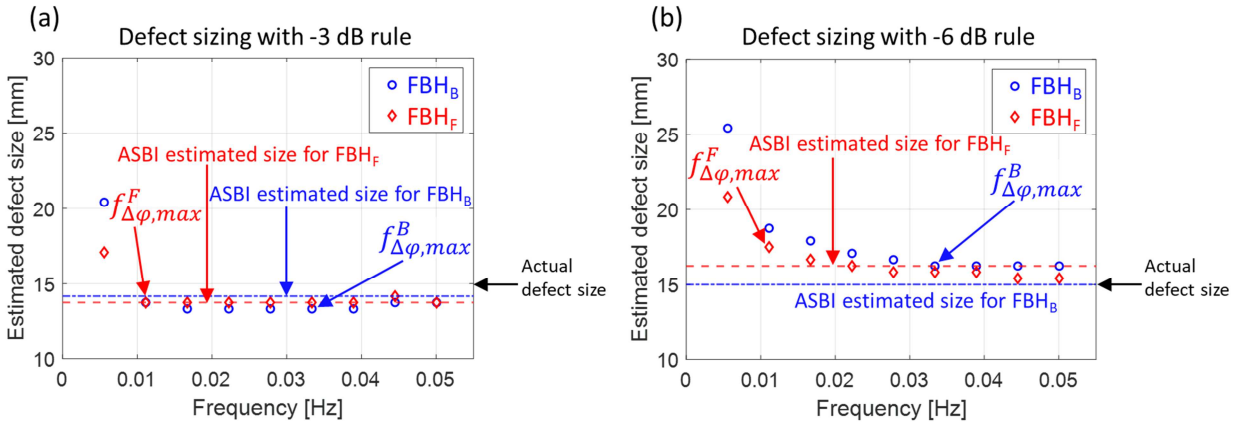

Figure 5: Estimation of the lateral size of FBH_B and FBH_F (see Figure 1(a)) in function of frequency based on the (a) -3 dB rule; and (b) -6 dB drop rule.

Since the -3 dB drop technique typically underestimated the defect sizes and the -6 dB drop technique overestimates them (see Figure 5), a more suitable threshold can be found somewhere between both values. Therefore, the amplitude drop is set to -4.5 dB (i.e. cut-off at 35% of the defect's maximum amplitude), for which the resulting defect size estimations are listed in Table 2. For this threshold, both PPT's optimal evaluation frequency $f_{\Delta\varphi,max}$ and ASBI provide accurate defect size estimations. The estimated defect size through ASBI shows low variations (error ranging between -6% and +3%) in comparison to those obtained by PPT's optimal evaluation frequency $f_{\Delta\varphi,max}$ (error ranging between -6% and +19%). These results suggest that the -4.5 dB drop technique is more appropriate for the inspected GFRP material than -3 dB or -6 dB, and that ASBI provides a more precise defect sizing than PPT's optimal evaluation frequency $f_{\Delta\varphi,max}$.

Journal Pre-proof

Table 2: Estimated defect sizes with the -4.5 dB drop technique for all FBHs of the GFRP sample with diameter of 15 mm (see Figure 1(a)) for PPT (at $f_{\Delta\varphi,max}$) and ASBI.

Estimated defect size with -4.5 dB rule [mm]
($\phi = 15$ mm)

	Depth [mm]	PPT (at $f_{\Delta\varphi,max}$)	ASBI		Depth [mm]	PPT (at $f_{\Delta\varphi,max}$)	ASBI
FBH_A	0.25	15.42 (+3%)	14.58 (-3%)	FBH_I	2.25	14.17 (-6%)	15 (0%)
FBH_B	0.5	15 (0%)	14.58 (-3%)	FBH_J	2.5	14.58 (-3%)	14.58 (-3%)
FBH_C	0.75	15.42 (+3%)	15 (0%)	FBH_K	2.75	14.17 (-6%)	14.17 (-6%)
FBH_D	1	15 (0%)	15 (0%)	FBH_L	3	16.25 (+8%)	14.58 (-3%)
FBH_E	1.25	15.42 (+3%)	15.42 (+3%)	FBH_M	3.25	17.92 (+19%)	15.42 (+3%)
FBH_F	1.5	16.25 (+8%)	15.42 (+3%)	FBH_N	3.5	17.08 (+14%)	15 (0%)
FBH_G	1.75	15.42 (+3%)	15 (0%)	FBH_O	3.75	15.83 (+6%)	15 (0%)
FBH_H	2	15 (0%)	15 (0%)	FBH_P	4	16.25 (+8%)	14.58 (-3%)

4.3. Performance comparison with thermal signal area

This section compares the performance of the proposed ASBI approach to a recently introduced technique called Thermal Signal Area (TSA) [22]. The TSA technique is similar to ASBI, but it performs an integration procedure in the temperature- time domain (instead of frequency-phase domain). Though, the integration limits for TSA ought to be treated with care in order to reduce the influence of noise and to have sufficient depth probing and accurate defect sizing. Indeed, a long evaluation period in TSA is needed to assess defects at different depths. Though, it will induce blurry edges for the shallow defects, due to an increased effect of lateral heat diffusion. A short evaluation time will mark shallow defects more clearly, but the detectability of deeper defects is then significantly reduced. Thus, there exists a tradeoff between shallow defect sharpness, and deep defect detectability. A proper choice of the temporal evaluation range is not straightforward without prior knowledge on the sample and its defects.

Different temporal ranges for the TSA have been evaluated, and for this specific GFRP sample with FBHs it was found that the temporal range of 0-50 s provides good TSA results (see Figure 6(a-b)). However, notice also that the non-uniform background (concentrated above the second column of FBHs from the left) is not removed by this technique due to the fact that it relies on evaluating temperature values in time domain. The ASBI approach, on the other hand, integrates the negative phase contrast within a suitable spectral range, which results in a strongly reduced background non-uniformity and noise level, and a significantly increased detectability of deep defects (see Figure 4(e)). This can also be observed in Figure 6(b), which displays a cross-sectional plot along line S-S' for both TSA and ASBI. The SNR values are indicated in Figure 6(b) for cross-section S-S' and in Table 1 for all FBHs, and are consistently higher for ASBI. Further, note that the proposed ASBI algorithm automatically determines the optimal frequency range for each pixel individually, thus making it user-independent.

The errors on the estimated defects sizes for TSA have not been added to Table 2 since the drop rule cannot effectively be applied due to the significant background non-uniformity.

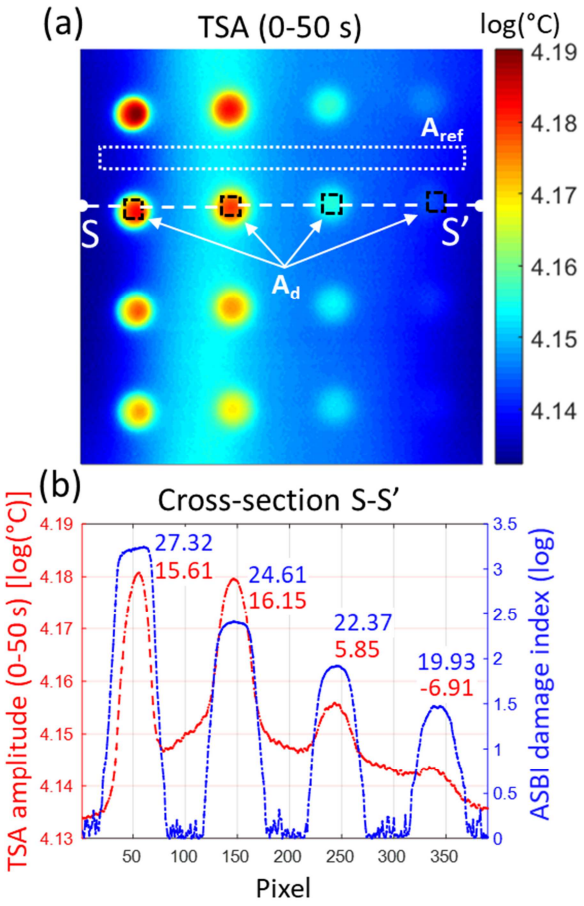

Figure 6: (a) Result of TSA for the temporal range 0-50 s; (b) Cross-section S-S' for TSA (0-50 s) and ASBI, with indications of the defects' SNR values (in dB).

5. ASBI and defect depth

In this section, it is first demonstrated for the experimental case on the GFRP sample that a trend can be observed between ASBI's damage index value and the defect depth. Next, the possibility for defect depth inversion is investigated through Finite Element (FE).

5.1. Defect depth quantification through ASBI

A careful evaluation of Figure 4(f) shows a trend between the damage index and the defect depth, which suggests the opportunity of defect depth quantification.

Additional experiments were performed for cross-ply $[(0/90)_5]_s$ GFRP samples with FBHs of diameter 5, 10 and 15 mm (see Section 2). In Figure 7, the calculated damage index by ASBI at the center of the FBHs (averaged over an area of 3x3 pixels) is plotted against the defect depth. The three deepest FBHs remained undetected for the diameter of 5 mm, while for the diameter of 10 mm only the deepest FBH at 4 mm depth was undetected. It is noteworthy that ASBI achieves at least the same minimum diameter-to-depth ratio for the GFRP with FBHs (i.e. 5 mm / 3.25 mm = 1.5) as what is reported in literature [4, 5, 29, 42, 43]. However, it should be noted that comparing different studies in terms of detectable diameter-to-depth ratio is not straightforward due to different measurement conditions. For each FBH diameter, a quadratic curve is fitted and the R^2 value of the fitted curve is calculated to assess the fitting quality. The R^2 value is a measure for the quality of the fit, and a value closer to 1.0 generally indicates a better fit. Since the R^2 value of each fitting is higher than 0.98, the quadratic relationship

represents the experimentally obtained data well. Figure 7 further indicates that the relationship between the defect depth and the damage index is affected by the size of the defect. With increasing defect depth, the smaller defects are more affected by lateral heat diffusion. This causes the slope of the damage index values to be higher for the smaller defects. There is of course an expected upper value on the FBH diameter, after which increasing the defect size further will no longer affect the damage index values. In the following section, the correlation between the damage index and the defect depth is further studied through FE simulations.

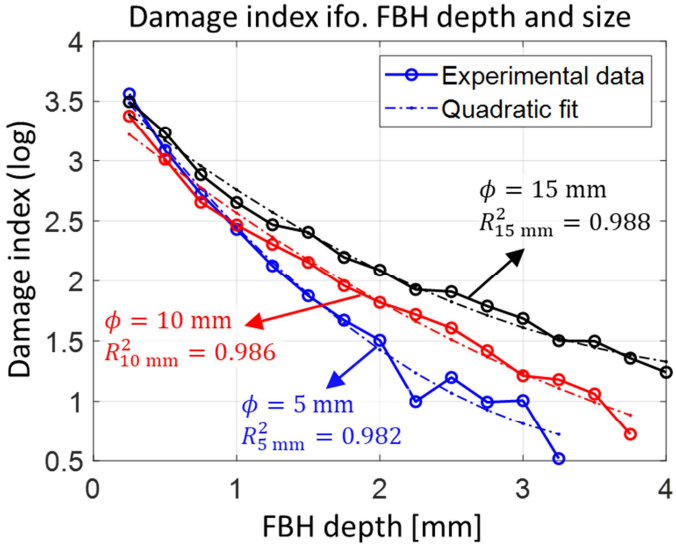

Figure 7: Damage index in function of FBH depth and diameter. A regression is performed on the experimental data points, the R^2 values are indicated in the figure.

5.2. FE and defect depth

In order to further study the depth inversion possibilities of ASBI, 3D finite element models (Abaqus/CAE) are set up in order to simulate the flash thermographic inspection of the GFRP samples with FBHs having a diameter of 5, 10 and 15 mm (see Figure 1(a) for a photograph of the sample with FBH diameter 15 mm). Care was taken to model each GFRP sample in an identical way to the experimentally inspected GFRP samples. The samples are modelled using 1.9×10^5, 1.2×10^5 and 2.6×10^5 brick elements, respectively, with temperature degree of freedom. The elements in the top two plies have quadratic shape functions (DC3D20) whereas the other plies have linear shape functions (DC3D8) [44], which provides accurate results for fast thermal events of the top surface while maintaining the calculation time within reasonable limits (2.5 hours on a cluster with 10 CPU's and 256 GB RAM). In order to obtain comparable results between FE and experiment, the thermal diffusivities of the GFRP sample were experimentally determined with the Hot Disk method (ISO 22007-2:2015, Ref. [45]). The following anisotropic thermal diffusivities were retrieved for a unidirectional lamina with the fibers along its X-direction: $\alpha_X = 4.11 \times 10^{-7} m^2/s$, $\alpha_Y = 2.93 \times 10^{-7} m^2/s$ and $\alpha_Z = 2.93 \times 10^{-7} m^2/s$. The optical excitation is modelled according to the actual flash lamp's parameters, i.e. 5 ms flash and 6 kJ energy. The modeled excitation provides a Gaussian-shaped heat flux, introducing a non-uniform surface heating [38]. The excitation is located at the center of the second row of defects (i.e. FBHs E, F, G and H), at a vertical elevation of 200 mm.

Next, white noise with different noise equivalent differential temperatures (NEDT) was added to the FE solution. The considered NEDT levels were defined based on typically used IR

Journal Pre-proof

cameras: 15 mK for cooled IR camera (used in this study), 45 mK for microbolometric IR camera, 150 mK for FLIR One Pro. The addition of each artificial noise level was iterated 10 times, after which the average values and standard deviations were calculated for the further discussions.

Figure 8(a) presents the output of ASBI for both the experimental case and the FE solution. It can be observed that there is a good match between the experiment (see also Figure 7) and the FE results for each FBH diameter and depth. Additionally, quadratic fits were calculated also for the FE results. The obtained R^2 values are 0.992, 0.987 and 0.992 for the FBHs of diameter 5, 10 and 15 mm, respectively. Thus, accurate calibration curves between ASBI's damage index and the defect depth can be constructed through the use of a straightforward FE model.

Figure 8(b) plots the effect of all considered NEDT levels (0 mK up to 150 mK) on the ASBI damage index in function of the defect depth for the FBH diameter of 15 mm (similar results were obtained for the FBHs with diameter of 5 and 10 mm). The calculated ASBI damage indices remain very stable for different levels of artificially added white noise. Only for the deepest defect at 4 mm depth, the damage index is somewhat affected for the high NEDT levels ($>$ 100 mK). Hence, these results indicate that ASBI provides a promising means for robust depth inversion, even under noisy conditions.

Alternatively, it was also verified how the depth inversion through the evaluation of the defect's second blind frequency $f_{blind,2}$ behaves for different noise levels (see Figure 8(c) for the FBH diameter of 15 mm). The results suggest that $f_{blind,2}$ is much more affected by measurement noise. Especially for shallow defects, an increase in noise significantly complicates the estimation of $f_{blind,2}$. Deeper defects are less influenced by the measurement noise, but still significantly more than ASBI's damage index. Remark that ASBI's damage index is dependent on the estimated $f_{blind,2}$ (see Eq. (1)), however, while the noise level strongly affects the estimated second blind frequency (see Figure 8(c)) for shallow defects, its underestimation does not contribute to any significant effect for ASBI's damage index (see Figure 8(b)). Notice also that the second blind frequencies $f_{blind,2}$ become stacked closer together with increasing defect depth (there are even repeating $f_{blind,2}$ values for the deep FBHs). This suggests that this indicator has a more limited depth estimation range than ASBI (for which deep defects still exhibit significantly different damage index values). The limiting factor is the frequency resolution Δf, which is inversely proportional to the recording duration t_d ($\Delta f = 1/t_d$). This was also observed in [14]. The used recording duration of 180 s can be considered quite long in flash thermography, but is still not sufficient for the second blind frequency approach to unambiguously distinguish between the deepest defects. Although a longer measurement increases the frequency resolution, it may not improve the defect detectability and may even worsen it by lateral heat diffusion. This is an inherent limitation of $f_{blind,2}$ which relies on a single frequency bin instead of the wideband information. Additionally, it should be remarked that the second blind frequency $f_{blind,2}$, which is used for depth inversion, shifts in function of the defect size (e.g. a smaller defect has a higher $f_{blind,2}$) [20]. This thus means that the defect's size affects PPT's depth estimation, like it also does in ASBI.

Journal Pre-proof

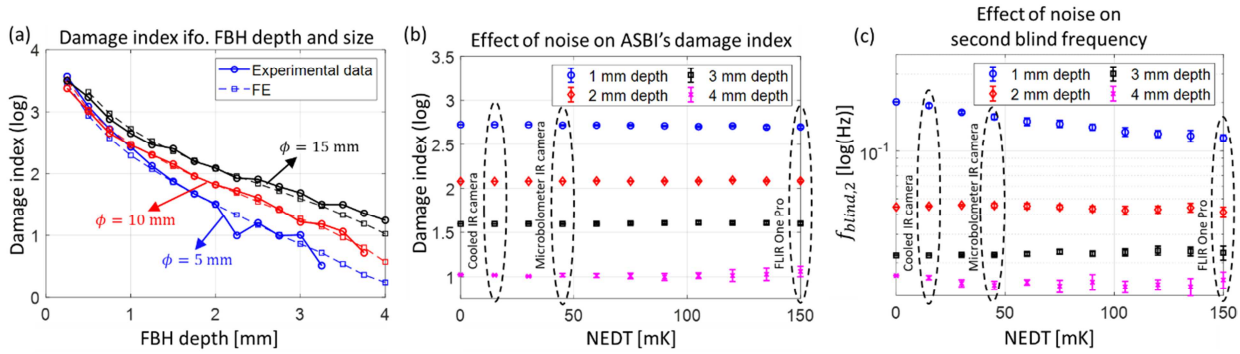

Figure 8: (a) Damage index in function of FBH depth and size for experiment and FE; (b,c) effect of measurement noise on ASBI's damage index and on the second blind frequency $f_{blind,2}$ for FBH diameter $\phi = 15$mm.

Next, the defect depths were estimated for the FBH diameters of 5, 10 and 15 mm by both PPT's second blind frequency $f_{blind,2}$ and for ASBI's damage index. For $f_{blind,2}$, the defect depth d is typically estimated based on its inverse relationship with the defect depth [9, 14, 35]:

$$d = C_1 \sqrt{\frac{\alpha}{\pi \cdot f_{blind,2}}} \tag{3}$$

where C_1 is a calibration variable typically set equal to 1.8 [9, 35] (as is done here) and α the through-thickness thermal diffusivity. For ASBI, calibration curves were constructed based on the FE solutions (see Figure 8(a)). An overview of all estimated defect depths of the experimentally investigated samples is provided in Table 3. For almost all combinations of the evaluated defect sizes and defect depths, ASBI provides a more precise defect depth estimation than $f_{blind,2}$. These results thus suggest that, for the presented GFRP samples, ASBI's damage index provides a more robust metric to perform quantitative defect depth inversion than PPT's second blind frequency $f_{blind,2}$. In order to perform defect depth inversion for other materials, an appropriate calibration should be constructed for this material based on FE results.

Table 3: Overview of the estimated defect depths for FBHs of 5, 10 and 15 mm diameter by PPT's second blind frequency $f_{blind,2}$ and ASBI's damage index (experimental results).

		Estimated defect depth [mm]											
	Depth [mm]	PPT (at $f_{blind,2}$)			ASBI			Depth [mm]	PPT (at $f_{blind,2}$)			ASBI		
		ϕ_5	ϕ_{10}	ϕ_{15}	ϕ_5	ϕ_{10}	ϕ_{15}		ϕ_5	ϕ_{10}	ϕ_{15}	ϕ_5	ϕ_{10}	ϕ_{15}
FBH_A	0.25	0.43 (+72%)	0.57 (+128%)	0.53 (+112%)	0.01 (-96%)	0.17 (-32%)	0.13 (-48%)	FBH_I	3.01 (+34%)	2.66 (+18%)	2.79 (+24%)	2.66 (+18%)	2.14 (-5%)	2.28 (+1%)
FBH_B	0.5	0.68 (+36%)	0.82 (+64%)	0.68 (+36%)	0.39 (-22%)	0.54 (+8%)	0.44 (-12%)	FBH_J	2.57 (+3%)	3.01 (+20%)	2.74 (+10%)	2.37 (-5%)	2.31 (-8%)	2.31 (-8%)
FBH_C	0.75	0.95 (+27%)	1.20 (+60%)	0.99 (+32%)	0.71 (-5%)	0.94 (+25%)	0.88 (+17%)	FBH_K	2.95 (+7%)	3.30 (+20%)	3.01 (+9%)	2.67 (-3%)	2.60 (-5%)	2.52 (-8%)
FBH_D	1	1.20 (+20%)	1.37 (+37%)	1.23 (+23%)	0.98 (-2%)	1.16 (+16%)	1.18 (+18%)	FBH_L	2.95 (-2%)	3.69 (+23%)	3.30 (+10%)	2.65 (-12%)	2.96 (-1%)	2.71 (-10%)
FBH_E	1.25	1.44 (+15%)	1.63 (+30%)	1.56 (+25%)	1.28 (+2%)	1.35 (+8%)	1.44 (+15%)	FBH_M	3.79 (+17%)	3.69 (+14%)	3.69 (+14%)	3.53 (+9%)	3.02 (-7%)	3.07 (-6%)
FBH_F	1.5	1.80 (+20%)	1.94 (+29%)	1.64 (+9%)	1.54 (+3%)	1.54 (+3%)	1.53 (+2%)	FBH_N	3.5	-	3.74 (+7%)	3.69 (+5%)	-	3.24 (-7%)	3.08 (-12%)
FBH_G	1.75	2.03 (+16%)	2.33 (+33%)	2.13 (+22%)	1.77 (+1%)	1.80 (+3%)	1.84 (+5%)	FBH_O	3.75	-	4.26 (+14%)	4.26 (+14%)	-	4.00 (+7%)	3.38 (-10%)
FBH_H	2	2.22 (+11%)	2.52 (+26%)	2.29 (+15%)	1.97 (-2%)	2.00 (0%)	2.01 (+1%)	FBH_P	4	-	-	4.26 (+6%)	-	-	3.66 (-8%)

Finally, a depth map through ASBI is calculated for the entire GFRP sample with FBHs of diameter 15 mm, which is presented in Figure 9(a). Additionally, this depth map allows to make slices through the sample's depth. The slice ranging from 2 to 3 mm depth (from the inspected surface) is displayed in Figure 9(b). All FBHs that are contained within this depth range (i.e. FBHs H, I, J, K and L) are clearly detected. Notice that artefacts from the outer parts of shallower defects are present. This is a result of the lateral heat diffusion that occurs predominantly at the lower evaluation frequencies, leading to a lower damage index value at the defects' boundaries. These defect edges are therefore estimated to be deeper than the center of the defect. This also explains why the apparent size of the defects in the slice reduces with increasing depth.

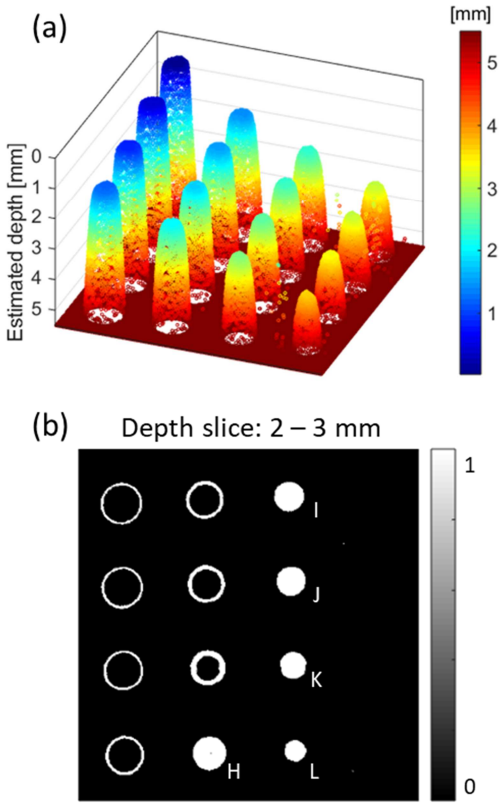

Figure 9: (a) Depth map through ASBI for the experimentally investigated GFRP sample with FBHs of diameter 15 mm (see Figure 1(a)); (b) slice of the depth map corresponding to the depth range 2-3 mm.

The accurate defect sizing by applying the -4.5 dB drop technique on ASBI's damage index map (see section 4.2) can be exploited to obtain a cleaner depth slice than in Figure 9(b). First, the -4.5 dB drop technique is applied on the damage index map in Figure 10(a), which results in the thresholded map presented in Figure 10(b). Next, for each FBH, the mean damage index area of the 5×5 pixel area at its center is assigned to the entire defected area. Notice that this assumes that the entire defected area is located at a single depth. This is a valid assumption for most defect types in the case of composites due to the layered structure (e.g. delaminations or inserts are located in between plies). However, for more complicated defect types that cover multiple plies (e.g. for a barely visible impact damage), this assumption would not be valid. Next, the defect sizes of the detected defects are extracted. Following, an enhanced depth map (see Figure 10(c)) can be constructed by applying an appropriate calibration for the defect (established through FE). For the selection of the appropriate calibration, it would be beneficial to priorly establish a calibration library of different defect shapes for the tested material. Lastly, enhanced depth slices can be made (see Figure 10(d) for the enhanced depth slice of 2 to 3 mm

Journal Pre-proof

depth). The defect size in this enhanced depth slice is significantly improved over the depth slice in Figure 9(b), and there are no artefacts from shallower defects.

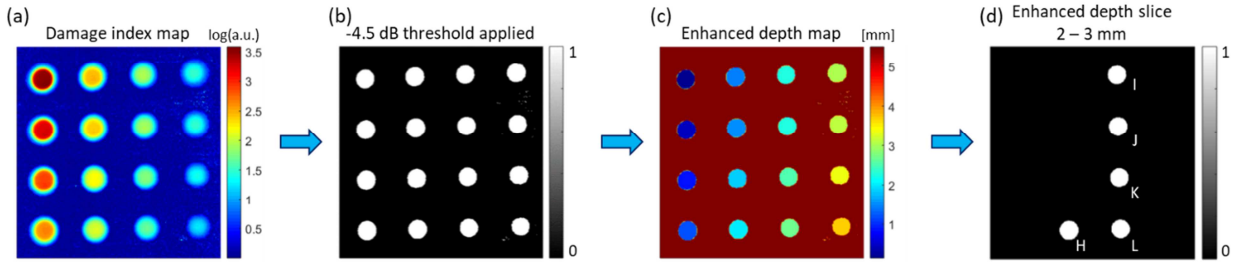

Figure 10: Procedure for enhanced depth slicing (applied on experimental results): (a) ASBI's damage index map; (b) thresholded map by applying the -4.5 dB drop technique; (c) enhanced depth map; and (d) enhanced depth slice corresponding to the depth range 2-3 mm.

6. Application of ASBI on complex defect cases

6.1. CFRP coupon with Barely Visible Impact Damage

The performance of ASBI is evaluated on the quasi-isotropic CFRP sample with BVID (see section 2 and Figure 1(b)). This is one of the typical defect types that may occur in composites, in which the defected region extends over several plies in the depth direction. In earlier studies by other researchers, impact damages have been investigated with infrared thermography both while the impact occurs [46, 47] and with lock-in thermography after their formation [46-48]. This is a particularly demanding inspection case considering the increased lateral heat diffusion in CFRP on the one hand, and the complex nature of BVID on the other hand. The results obtained with ASBI are benchmarked with the ultrasonic C-scan since this is currently the industrial standard. Both sides of the impacted sample were inspected with both techniques.

The ultrasonic C-scans were performed with a focused 5 MHz transducer in reflection mode with dynamic time-gating, after which the obtained data was post-processed to obtain relative amplitude and time-of-flight (TOF) images (see Figure 11(a-d)). The impact induces a delamination cone [37] which resembles the shape of a winding staircase with steps every 45°. For the C-scan on the back side, also a second level of the winding staircase can be observed on the lower-left. The TOF images give quantitative information on the defect depth of the different delaminations that were introduced by the impact. It is clear that proper detection and assessment for this defect type is highly challenging. The defect edges are highlighted on the C-scan images in order to provide a means of comparison with the thermographic results.

The sample was also inspected using flash thermography, with the experimental setup as described in section 2. Firstly, the raw thermographic sequences were carefully inspected, and it was observed that the raw datasets are insufficient for proper defect detection. Then, the recorded data sequences were post-processed by PPT, for which phase contrast maps at 0.51 Hz and 0.13 Hz are presented in Figure 11(e-h). At a relatively high frequency (Figure 11(e,f)), only the first steps of the staircase are clearly detected, while the deeper steps are completely absent. At a lower frequency (see Figure 11(g,h)), the different steps of the delamination cone merge together due to the increased effect of the lateral heat diffusion.

Next, the recorded flash thermographic sequences are fed to the ASBI algorithm, for which the damage index maps are displayed in Figure 11(i,j). For the impacted side, the first four steps are detected and compare well with the corresponding C-scan images, while deeper steps are less

distinguishable. Notice that the background is almost completely removed in the damage index map, providing a sharp edge of the defected area, which is comparable to the one highlighted by the C-scan results. For the back side, the first level of the winding staircase is clearly detected in a qualitative manner, and shows good correspondence with the results of the C-scan images. Even the second level of the winding staircase can be observed, although the different steps are merged together for this level. In general, the ASBI damage index map separates the different steps up to a deeper depth than the individual PPT phase contrast images and strongly improves the background uniformity. Moreover, the transition area from one step to the next, and from the defect to the surrounding sound area, is smooth in the PPT phase images (due to 3D heat diffusion), while ASBI makes sharper edges for the shallow parts of this complex defect. For the back side, the second level of the winding staircase was not clearly detected by PPT (all frequencies have been carefully checked). ASBI on the other hand provided a clear detection of this deep second level of delaminations.

While qualitative depth information is available in the damage index map, quantitative depth inversion through ASBI was not successful. This is attributed to three main reasons. Firstly, this is a result of the complexity of the BVID, where the delaminations are in close proximity of each other and their depths are very similar. This thus leads to thermal interactions between the different layers of the BVID, making quantitative depth retrieval very challenging. Secondly, the much higher in-plane thermal diffusivity of CFRP, compared to GFRP, leads to discrepancies with the established calibration. Thirdly, the FE depth calibration curves have only been computed for the simple FBH defects. Modelling such a complex defect like BVID, with delaminations and matrix cracks, is far from straightforward.

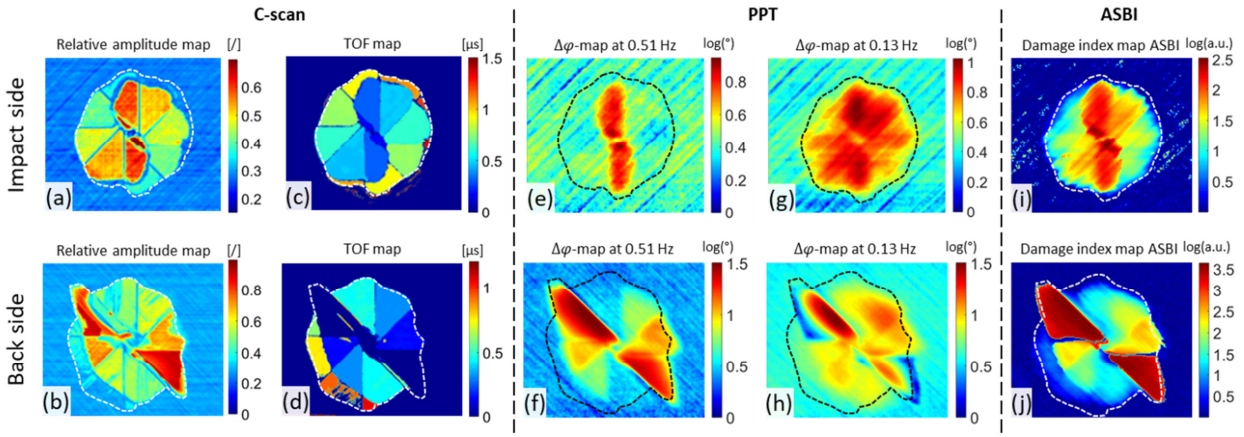

Figure 11: Impacted side (top row) and back side (bottom row) of the impacted CFRP: (a-d) C-scan relative amplitude and TOF; (e-f) PPT phase contrast image at 0.51 Hz; (g-h) PPT phase contrast image at 0.13 Hz; and (i,j) ASBI damage index map.

6.2. Stiffened CFRP aircraft component with a complex cluster of production defects

Lastly, the performance of ASBI is evaluated on a CFRP aircraft panel (Airbus A400M lower flap) with backside stiffeners and production defects (see section 2 and Figure 1(c)). Due to the complexity of the production process of such components, a wide range of possible defects (porosities, resin rich areas, inclusions, fiber wrinkling, …) may be accidentally introduced into the specimen during manufacturing. Considering the criticality of these components, accurate non-destructive inspection is needed for all parts. This component provides an increased inspection challenge due to the non-uniform thickness at the backside stiffeners. As mentioned in section 2, only the region around the defected area (~200x160 mm^2) is inspected due to the

availability of only one flash lamp. Firstly, the phase contrast maps at 0.13 Hz and 0.05 Hz are displayed in Figure 12(a,b), in which two backside stiffeners with several distortions in between them can be clearly observed. At 0.13 Hz, the background is quite non-uniform and noisy, and does not allow for straightforward extraction of all parts of the complex defect cluster. At 0.05 Hz, the background noise is significantly reduced, but the detectability of the smaller defects remains unclear. The damage index map obtained by ASBI is displayed in Figure 12(c). Two bands of high damage indices are clearly observed, which correspond to the backside stiffeners (locally increased thickness). Apart from this, local increased damage index values are retrieved which provide clear indications of a complex cluster of manufacturing defects (see hatched area in Figure 1(c)). Both large defects and very small ones are highlighted with ASBI, and the background non-uniformity and noise level are strongly reduced. Two extra zones are also highlighted by ASBI (encircled in red in Figure 12(c)), however, these were intentionally introduced during manufacturing in order to aid the placement of the stiffeners, and are thus in principle no defects. The obtained damage index map showed good correspondence with other NDT techniques. These results indicate that the effectiveness of ASBI is not limited to the inspection of coupon samples, but that the technique is also applicable to more complex industrial samples.

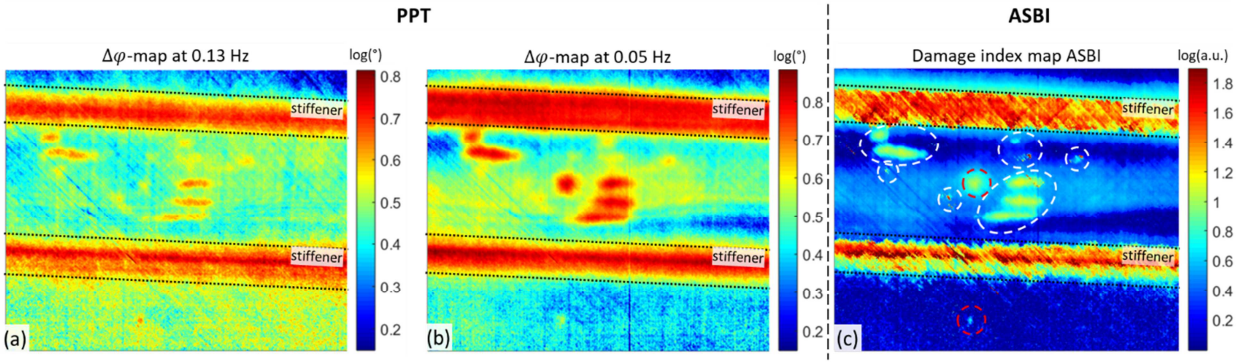

Figure 12: (a,b) Phase contrast map at 0.13 Hz and 0.05 Hz; and (c) Damage index map of ASBI for an aircraft component with backside stiffeners and production defects.

7. Conclusions

In this paper, a novel data post-processing technique for flash thermography, called Adaptive Spectral Band Integration (ASBI), is introduced. In this technique, the phase contrast is integrated over the relevant frequency range in a pixel-wise manner. The ASBI approach does not require any user input (or parameter selection), nor does it require a priori information on the sample or defect. The performance of ASBI has been demonstrated on a GFRP sample with FBHs of different diameters (5, 10 and 15 mm) and depths (0.25-4 mm). The results show that the ASBI approach significantly increases the SNR while effectively suppressing effects of non-uniform heating, background reflections and surface non-uniformities. Its high robustness to measurement noise is illustrated, and ASBI obtains an almost zero-reference background. Additionally, with the support of FE simulations, it is shown that ASBI can be used for accurate defect sizing as well as for quantitative depth estimation. The performance of ASBI has been extensively compared to both Pulsed Phase Thermography and Thermal Signal Area, and it was found to provide a higher defect detectability and an improved metric for quantitative defect assessment (sizing and depth estimation).

ASBI has also been applied on more challenging inspection cases. The results on a CFRP coupon with Barely Visible Impact Damage showed its good performance in detecting and sizing the

Journal Pre-proof

complex structure of the BVID defect. Good agreement was found with the ultrasonic C-scan inspection. However, due to the increased lateral heat diffusion effects in CFRP and the complex structure of BVID, quantitative depth inversion was not successful. The performance of ASBI has been further demonstrated on an aircraft CFRP panel (Airbus A400M) with backside stiffeners and a complex cluster of production defects. Apart from highlighting the backside stiffeners, it was also successful in retrieving the cluster of production defects while reducing measurement noise and background non-uniformity.

In conclusion, ASBI is a simple yet effective data post-processing method for flash thermography which can handle demanding inspection conditions (noise, complex defect, industrial part). The fact that it produces a single high-quality damage index map, makes it attractive as input for unsupervised automated defect detection algorithms.

Acknowledgement

The authors acknowledge the SBO project DETECT-IV (Grant no. 160455), which fits in the SIM research program MacroModelMat (M3) coordinated by Siemens (Siemens Digital Industries Software, Belgium) and funded by SIM (Strategic Initiative Materials in Flanders) and VLAIO (Flemish government agency Flanders Innovation & Entrepreneurship). The authors also acknowledge Fonds voor Wetenschappelijk Onderzoek-Vlaanderen (FWO-Vlaanderen) through grants 1S11520N, 1148018N and 12T5418N. The authors further thank SABCA Limburg for providing the CFRP aircraft panel for this investigation.

References

1. Ciampa, F., et al., *Recent Advances in Active Infrared Thermography for Non-Destructive Testing of Aerospace Components.* Sensors (Basel), 2018. **18**(2).
2. Milne, J.M. and W.N. Reynolds, *The non-destructive evaluation of composites and other materials by thermal pulse video thermography.* Thermosense VII, 1985: p. 119-1222.
3. Yang, R. and Y. He, *Optically and non-optically excited thermography for composites: A review.* Infrared Physics & Technology, 2016. **75**: p. 26-50.
4. Maierhofer, C., et al., *Evaluation of Different Techniques of Active Thermography for Quantification of Artificial Defects in Fiber-Reinforced Composites Using Thermal and Phase Contrast Data Analysis.* International Journal of Thermophysics, 2018. **39**(5).
5. Maierhofer, C., et al., *Characterizing damage in CFRP structures using flash thermography in reflection and transmission configurations.* Composites Part B: Engineering, 2014. **57**: p. 35-46.
6. Ibarra-Castanedo, C., et al., *Infrared image processing and data analysis.* Infrared Physics & Technology, 2004. **46**(1-2): p. 75-83.
7. Poelman, G., et al., *Multi-scale gapped smoothing algorithm for robust baseline-free damage detection in optical infrared thermography.* NDT & E International, 2020. **112**.
8. Erazo-Aux, J., L.-C. H, and A.D. Restrepo-Giron, *Histograms of oriented gradients for automatic detection of defective regions in thermograms.* Applied Optics, 2019. **58**(13): p. 3620-3629.
9. Ibarra-Castanedo, C., et al., *On signal transforms applied to pulsed thermography.* Recent Res. Devel. Applied Phys., 2006. **9**.
10. Vavilov, V.P. and D.D. Burleigh, *Review of pulsed thermal NDT: Physical principles, theory and data processing.* NDT & E International, 2015. **73**: p. 28-52.
11. Wang, Z., et al., *Image processing based quantitative damage evaluation in composites with long pulse thermography.* NDT & E International, 2018. **99**: p. 93-104.
12. Zheng, K., Y.-S. Chang, and Y. Yao, *Defect detection in CFRP structures using pulsed thermographic data enhanced by penalized least squares methods.* Composites Part B: Engineering, 2015. **79**: p. 351-358.
13. Maldague, X. and S. Marinetti, *Pulse phase infrared thermography.* Journal of Applied Physics, 1996. **79**(5): p. 2694-2698.
14. Ibarra-Castanedo, C. and X. Maldague, *Pulsed phase thermography reviewed.* Quantitative InfraRed Thermography Journal, 2004. **1**(1): p. 47-70.

Journal Pre-proof

15. Benítez, H.D., et al., *Definition of a new thermal contrast and pulse correction for defect quantification in pulsed thermography.* Infrared Physics & Technology, 2008. **51**(3): p. 160-167.
16. Pilla, M., et al. *New Absolute Contrast for pulsed thermography*. in *Proceedings of the 2002 International Conference on Quantitative InfraRed Thermography*. 2002.
17. Rajic, N. and DSTO-TR-1298, *Principal Component Thermography*. 2002, Defence Science and Technology Organisation Victoria (Australia) Aeronautical and Maritime Research Lab. p. 38.
18. Shepard, S.M., *Temporal noise reduction, compression and analysis of thermographic data sequences*. 2003, Thermal Wave Imaging, Inc.: US.
19. Balageas, D.L., et al., *The Thermographic Signal Reconstruction Method: A Powerful Tool for the Enhancement of Transient Thermographic Images.* Biocybern Biomed Eng, 2015. **35**(1): p. 1-9.
20. Oswald-Tranta, B., *Time and frequency behaviour in TSR and PPT evaluation for flash thermography.* Quantitative InfraRed Thermography Journal, 2017. **14**(2): p. 164-184.
21. Vavilov, V.P. and M.V. Kuimova, *Dynamic Thermal Tomography of Composites: A Comparison of Reference and Reference-Free Approaches.* Journal of Nondestructive Evaluation, 2018. **38**(1).
22. Moradi, M. and M.S. Safizadeh, *Detection of edge debonding in composite patch using novel post processing method of thermography.* NDT & E International, 2019. **107**: p. 102153.
23. Saintey, M.B. and D.P. Almond, *Defect sizing by transient thermography II: a numerical treatment.* J Phys D Appl Phys, 1995. **28**: p. 2539-2546.
24. Choi, M., et al., *Quantitative determination of a subsurface defect of reference specimen by lock-in infrared thermography.* NDT & E International, 2008. **41**(2): p. 119-124.
25. Kumaran, S. and S. Rani.B, *Application of 6db Drop Technique to Estimate the Width of Sub Assembly Ring Top Using Pulse Echo Ultrasonic Technique.* International Journal of Engineering and Technology, 2013. **5**(6).
26. Ciorau, P., *Comparison between -6 dB and -12 dB amplitude drop techniques for length sizing.* ndt.net, 2011, no. 4.
27. Murphy, R.V., *Ultrasonic defect-sizing using decibel drop methods: Volume I: Text*. 1987, Atomic Energy Control Board: Ottawa, Canada.
28. Theodorakeas, P. and M. Koui, *Depth Retrieval Procedures in Pulsed Thermography: Remarks in Time and Frequency Domain Analyses.* Applied Sciences, 2018. **8**(3).
29. Sun, J.G., *Analysis of Pulsed Thermography Methods for Defect Depth Prediction.* Journal of Heat Transfer, 2006. **128**(4).
30. Vavilov, V., V. Shiryaev, and M. Kuimova, *Time- and Phase-Domain Thermal Tomography of Composites.* Photonics, 2018. **5**(4).
31. Moskovchenko, A.I., V.P. Vavilov, and A.O. Chulkov, *Comparing the efficiency of defect depth characterization algorithms in the inspection of CFRP by using one-sided pulsed thermal NDT.* Infrared Physics & Technology, 2020.
32. Chulkov, A.O., et al., *Optimizing input data for training an artificial neural network used for evaluating defect depth in infrared thermographic nondestructive testing.* Infrared Physics & Technology, 2019. **102**.
33. Dudzik, S., *Two-stage neural algorithm for defect detection and characterization uses an active thermography.* Infrared Physics & Technology, 2015. **71**: p. 187-197.
34. Alvarez-Restrepo, C.A., H.D. Benitez-Restrepo, and L.E. Tobón, *Characterization of defects of pulsed thermography inspections by orthogonal polynomial decomposition.* NDT & E International, 2017. **91**: p. 9-21.
35. Meola, C. and G.M. Carlomagno, *Recent advances in the use of infrared thermography.* Measurement Science and Technology, 2004. **15**(9): p. 27-58.
36. Bai, W. and B.S. Wong, *Evaluation of defects in composite plates under convective environments using lock-in thermography.* Measurement Science and Technology, 2001. **12**(2): p. 142-150.
37. Spronk, S.W.F., et al., *Comparing damage from low-velocity impact and quasi-static indentation in automotive carbon/epoxy and glass/polyamide-6 laminates.* Polymer Testing, 2018. **65**: p. 231-241.
38. Hedayatrasa, S., et al., *Performance of frequency and/or phase modulated excitation waveforms for optical infrared thermography of CFRPs through thermal wave radar: A simulation study.* Composite Structures, 2019. **225**.
39. Madruga, F.J., et al., *Infrared thermography processing based on higher-order statistics.* NDT & E International, 2010. **43**(8): p. 661-666.
40. Zhang, H., et al., *Enhanced Infrared Image Processing for Impacted Carbon/Glass Fiber-Reinforced Composite Evaluation.* Sensors (Basel), 2017. **18**(1).
41. Usamentiaga, R., et al., *Nondestructive Evaluation of Carbon Fiber Bicycle Frames Using Infrared Thermography.* Sensors (Basel), 2017. **17**(11).

Journal Pre-proof

42. Ibarra-Castanedo, C. and X. Maldague, *Defect Depth Retrieval from Pulsed Phase Thermographic Data on Plexiglas and Aluminum Samples.* SPIE Proceedings Thermosense XXVI, 2004. **5405**.
43. Lau, S.K., D.P. Almond, and J.M. Milne, *A quantitative analysis of pulsed video thermography.* NDT & E International, 1991. **24**(4): p. 195-202.
44. Hedayatrasa, S., et al. *On Efficient FE Simulation of Pulse Infrared Thermography for Inspection of CFRPs*. in *14th Quantitative InfraRed Thermography Conference (QIRT 2018)*. 2018. Berlin, Germany.
45. *ISO 22007, Plastics — Determination of thermal conductivity and thermal diffusivity — Part 2: Transient plane heat source (hot disc) method*. 2015.
46. Meola, C., et al., *Impact damaging of composites through online monitoring and non-destructive evaluation with infrared thermography.* NDT & E International, 2017. **85**: p. 34-42.
47. Meola, C. and G.M. Carlomagno, *Infrared thermography to evaluate impact damage in glass/epoxy with manufacturing defects.* International Journal of Impact Engineering, 2014. **67**: p. 1-11.
48. Boccardi, et al., *Lock-In Thermography and Ultrasonic Testing of Impacted Basalt Fibers Reinforced Thermoplastic Matrix Composites.* Applied Sciences, 2019. **9**(15).

Journal Pre-proof

Journal Pre-proof

Declaration of interests

☒ The authors declare that they have no known competing financial interests or personal relationships that could have appeared to influence the work reported in this paper.

☐The authors declare the following financial interests/personal relationships which may be considered as potential competing interests:

Journal Pre-proof